AIAA JOURNAL
Vol. 38, No. 4, April 2000

# Molecular Dynamics Study on Mechanical Properties and Fracture in Amorphous Metal

Keiko Nakatani*
*Osaka Prefecture University, Osaka 599-8531, Japan*
Akihiro Nakatani†
*Osaka University, Osaka 565-0871, Japan*
Yoshihiko Sugiyama‡
*Osaka Prefecture University, Osaka 599-8531, Japan*
and
Hiroshi Kitagawa§
*Osaka University, Osaka 565-0871, Japan*

**The dynamics of atomic arrangement observed on a microscopic scale in amorphous iron are analyzed in detail to obtain the mechanical properties and fracture mechanisms of amorphous metal. First, an amorphous model specimen created by a melting and rapid-quenching process by computer simulation is tested by molecular dynamics (MD) under uniaxial preloading and subsequent biaxial reloading. This process can directly deal with phenomena at atomic scale. The results of the simulation show that the initial properties of the model are recovered even if it is subjected to strains closely approaching the maximum loading point. However, further excess loading causes a change of atomic structure and a remarkable decrease of its elastic modulus and yield stress. Next, the MD simulations of mode I crack propagations are carried out. The $J$ integral, one of the representative mechanical parameters often used as a criterion of crack propagation in continuum mechanics, is evaluated. The changes of mechanical properties are concerned with the material damage and the geometrical nonlinearity of a blunted tip, which may be predicted quantitatively by using $J^*$ integral that is evaluated by choosing the appropriate integral region.**

## I. Introduction

AMORPHOUS metal is known to have various notable features including a high yielding point and high ductility.[1,2] Theoretical and experimental attempts to obtain mechanisms of both deformation and fracture in amorphous metal have been difficult because of its atomic order random structure. Recently, computer performance has improved to the point where we can now study phenomena that were not accessible to theoretical and experimental approaches. Using computer simulations such as molecular dynamics (MD) we can deal directly with phenomena of an atomic order. In this way we can now investigate not only atomistic behaviors during very short periods, but also macroscopic properties.

In this paper, the results of a series of computer simulations of amorphous metal are reviewed. The paper addresses three topics.

The first is a simulation of a melting and rapid-quenching process of BCC iron atoms using the MD method to obtain an amorphous structure. It is certified at various points that the obtained structure is a stable amorphous structure.

The second is a simulation to test strength under uniaxial and biaxial preloading/reloading conditions to clarify fundamental mechanical properties. The elastic moduli and yielding stress are evaluated by the stress–strain curves obtained by tensile and compressive loading. We also discuss the damage by tensile preloading, which is observed as a decrease of elastic moduli and yield stress.

The third topic, the main focus of our report, is a simulation of fracture of amorphous metal. The mechanical properties of the field near the crack tip are examined using the MD method. The results are analyzed using conventional fracture mechanics, a useful tool for evaluation of material properties near the crack tip. Moreover, an atomistic parameter is proposed that corresponds to the conventional $J$ integral, a representative mechanical parameter commonly used as a criterion of crack propagation in continuum mechanics. The proposed parameter is evaluated in an atomistic simulation. It is shown that the mechanical state near the crack tip can be predicted quantitatively using the $J^*$ integral.

## II. Analytical Model and Methodology

### A. MD and Atomic Interaction

All of the atomistic problems mentioned in the Introduction are approached using the MD method.[3] In a MD simulation, the behavior of atoms that construct the simulation system is assumed to be governed by classical mechanics based on Newtonian equations of motion as follows:

$$m^{(\alpha)}\frac{\mathrm{d}^2\boldsymbol{q}^{(\alpha)}}{\mathrm{d}t^2} = -\frac{\partial\phi}{\partial\boldsymbol{q}^{(\alpha)}} \equiv \boldsymbol{F}^{(\alpha)}(t) \qquad (\alpha = 1, 2, \ldots, N) \quad (1)$$

where $m^{(\alpha)}$ is the mass of the $\alpha$th atom, $\boldsymbol{q}^{(\alpha)}$ is the position vector, and $\phi$ is potential energy of the system. $\boldsymbol{F}^{(\alpha)}(t)$ is the atomic interaction from other atoms at a time $t$, which is decided by the arrangement of atoms.

In the simulation, the initial value problems are calculated to solve the second-order simultaneous differential equations. Initial velocities are given to satisfy the Maxwellian distribution corresponding to the temperature of the system. In this study, we use the (NVE) ensemble, the (Nph) ensemble, and both forms mixed. Equations (1) are established for the (NVE) ensemble, and substitutions of variables and additional terms in Eq. (1) are necessary for others.

As the potential energy, we assume interaction according to Finnis–Sinclair (FS) potential as proposed in Refs. 4 and 5. This potential includes not only atomic pair interaction but also an $N$-body effect. It constructs a stable BCC iron structure at room temperature.

Presented as Paper 98-1815 at the AIAA/ASME/ASCE/AHS/ASC 39th Structures, Structural Dynamics, and Materials Conference, Long Beach, CA, 20–23 April 1998; received 29 September 1998; revision received 29 August 1999; accepted for publication 3 September 1999. 

*Research Associate, Department of Aerospace Engineering, College of Engineering, 1-1, Gakuen-cho, Sakai. Member AIAA.
†Associate Professor, Department of Adaptive Machine Systems, Graduate School of Engineering, 2-1, Yamadaoka, Suita.
‡Professor, Department of Aerospace Engineering, College of Engineering, 1-1, Gakuen-cho, Sakai. Member AIAA.
§Professor, Department of Adaptive Machine Systems, Graduate School of Engineering, 2-1, Yamadaoka, Suita.

### B. Generation of Amorphous Model

In applying an MD simulation to the process in which a perfect crystalline material is melted and quenched, we use Parrinello and Rahman's algorithm[6] to keep pressure constant.

The origin is positioned at a lattice point of the BCC structure that is the most stable configuration at ordinary temperature; $x$, $y$, and $z$ axes are taken in the [100], [010], and [001] directions, respectively; and a cube with a side of 17.2 Å $=6a$ ($a=2.8665$ Å is the lattice constant) is given as the fundamental cell.

In the present study, it is proved that coordinate axes expand or contract isotropically and do not rotate by averaging normal stress along each axis as

$$p=(\sigma_x+\sigma_y+\sigma_z)/3 \tag{2}$$

By assuming the periodic boundary condition in all directions, we can deal virtually with a system of infinite size. A model and conditions of the analysis are shown in Table 1. The temperature is controlled by scaling of velocity as shown in Fig. 1. The system in a crystalline state at the initial temperature $T_0=300$ K is heated continuously in region a at the rate $\dot{T}=10^{14}$ K/s to a sufficiently high temperature $T_1=5100$ K. In region b, the system is maintained at the control temperature of 5100 K during 4 ps. Afterward, the system is left free during 4 ps without temperature control in region c. In region d, we perform analysis of two cases of rapid quenching: Case 1 is $\dot{T}=-10^{14}$ K/s, and case 2 is $\dot{T}=-10^{13}$ K/s.

After rapid quenching down to 300 K, relaxation is performed in region e for 4 ps without temperature control to obtain a stable atomic configuration. Finally, in regions f and g, we cease to average the stress according to Eq. (2) and perform relaxation without temperature control during 4 and 40 ps, respectively, while permitting each axis to expand or contract but not to rotate.

The procedure of uniaxial tensile testing is described next. As testing material, we use the atomistic structure obtained by means of the already mentioned procedure. That it shows some properties of amorphous metal will be described in a later section. The three axes of coordinates $x$, $y$, and $z$ are set as shown in Fig. 2, to refer to the generated amorphous structure.

The structure is first subjected to a tensile load along a uniaxial direction ($y$ direction), which we call preloading. The loading state along a direction is controlled by assignment of the size of a cell. The size of cells along the remaining directions is kept in a stress-free state by Parrinello and Rahman's algorithm.[6] The loads are unloaded at certain points on the loading path to evaluate the mechanical properties of the material models that received the various levels of preloading. The increasing deformation is stopped at points on the loading path, and the deformation is controlled inversely. That is, on certain points along the loading path, the length of the side along the $y$ axis of a unit cell decreases at a constant rate. After unloading and relaxation, uniaxial or biaxial tensile load is again applied to these models; this is referred to as reloading.

The specified strain rate of the preloading is about $10^{10}$ s$^{-1}$, which corresponds to 20 m/s of the relative velocity between cell edges. In the reloading process, biaxial tensions in various stress ratios are applied by choosing a combination of the relative velocities between cell edges in the $x$ and $y$ directions from 5, 10, 15, and 20 m/s.

**Table 1 Model of analysis**

| Parameter | Value |
|---|---|
| Number of atoms | $N=432$ |
| Size of unit cell | $17.2\times17.2\times17.2$ Å |
| Initial temperature | 300 K |
| Interatomic potential | FS potential |
| Mass of Fe atom | $0.927376\times10^{-24}$ kg |
| Increment of time step | $2.0\times10^{-15}$ s |
| External stress | $1.0\times10^{5}$ Pa |

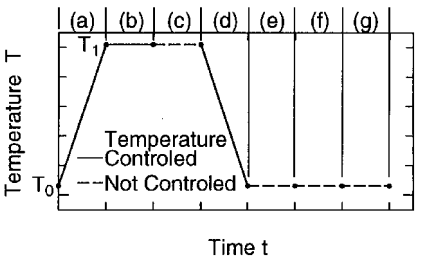


**Fig. 1 Control of temperature: a) heating, b) fixed temperature, c) isotropic relaxation, d) rapid quenching, e) isotropic relaxation, f) anisotropic relaxation 1, and g) anisotropic relaxation 2.**

**Table 2 Analytical models**

| Model | $K_I$, MPa$\sqrt{\text{m}}$ | $(J=\mathcal{G})$, Pa·m | Model | $K_I$, MPa$\sqrt{\text{m}}$ | $(J=\mathcal{G})$, Pa·m |
|---|---|---|---|---|---|
| C | 0.6062 | 2.337 | D | 0.7072 | 3.181 |
| E | 0.7578 | 3.652 | F | 0.8588 | 4.691 |
| G | 1.0103 | 6.492 | H | 1.2629 | 10.144 |
| I | 1.5155 | 14.608 | J | 1.6670 | 17.675 |
| K | 1.7681 | 19.883 | L | 1.9196 | 23.437 |

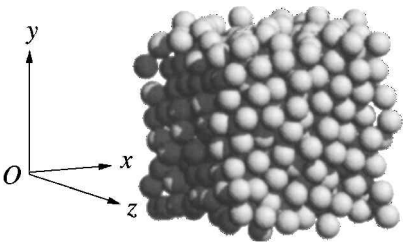


**Fig. 2 Initial structure of amorphous model.**

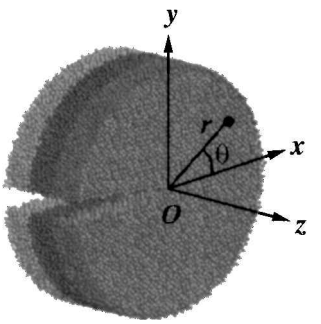


**Fig. 3 Initial arrangement of model C.**

### C. Crack Models and Method of Analysis

The model near the crack tip is a cylindrical region (radius $r=69.9$ Å) that consists of 22,251 atoms and is cut out from the atomic system that consists of the periodic unit cells, which is generated by means of the heating and rapid-quenching procedure mentioned in the preceding section. The periodic boundary condition is used along the crack front direction $z$, and the periodic length along $z$ direction is $l_z=17.6$ Å.

A crack is introduced into the model by atomic displacement that is obtained by the linear elastic solution with an initially specified stress intensity factor and the elastic properties (Young's modulus $E=146.4$ GPa and Poisson's ratio $\nu=0.26$) that are brought about by the simulation of uniaxial tensile deformation. From model C to model L, 10 cases examined in which the initial stress intensity factor is set as shown in Table 2. Within the linear elasticity, the value of the $J$ integral is equivalent to the energy release rate $\mathcal{G}$. It is expressed under the plane strain condition by

$$J=\mathcal{G}=(1-\nu^2)K_I^2/E \tag{3}$$

$J$ integrals that correspond with the stress intensity factors are also shown in Table 2. As mentioned in a later section, $K_I$ and $J$ in Table 2 indicate nominal values that differ from true values. The initial arrangement of model C is shown in Fig. 3. The bulk model, model B, which has no crack, and the surface model, model S, in which there are no atomic interactions across $xz$ plane, are calculated

by the same procedure. Model S is used to evaluate purely contributions of surface effects (surface energy and stress). They will be used for reference models.

An MD simulation for relaxation is carried out during 8 ps under the condition in which 2206 atoms within the range $r_c = 3.57$ Å from the outside surface are fixed. The potential energy density $W^{(\alpha)}$, atomic stress $\sigma_{ij}^{(\alpha)}$, and displacement $u_i^{\alpha}$ at the location of each atom are calculated and averaged at each time step during the final picosecond.

The atomic stress $\tau_i^{\alpha\beta}$, the $\alpha\beta$ component of the stress tensor ($\alpha, \beta = 1, 2, 3$) at atomic site $i$, is evaluated by using the interactions between neighbor atom $j$ (where $i, j = 1, 2, \ldots, N$), and it is expressed as follows:

$$\tau_i^{\alpha\beta} = \frac{1}{\Omega}\left[-m_i v_i^{\alpha} v_i^{\beta} + \frac{1}{2}\sum_{\substack{j=1 \\ j\neq i}}^{\text{neighbors}} V'_{\text{eff}}(q_{ij})\frac{q_{ij}^{\alpha} q_{ij}^{\beta}}{q_{ij}}\right] \tag{4}$$

where $V_{\text{eff}}(r)$ and $V'_{\text{eff}}(r)$ are an effective potential and its derivative function, respectively; $q_{ij}^{\alpha}$ is the $\alpha$ component of interatomic vector $\boldsymbol{q}_{ij}$; and $\Omega$ is the volume per atom. The volume per atom in the amorphous state is usually larger than in the perfect crystalline state, and it changes during deformation. Thus, for the sake of simplicity of the definition, we use the volume in the perfect crystalline state as $\Omega$. We consider the stress in each atom in a later section.

### 1. J *Integral in Atomic Model*

When we study the fundamental phenomena of fracture by means of atomistic simulation, we can use only these simulation results to discern macroscopic parameters. For simplicity, in an atomistic simulation of fracture, external forces or displacement of the boundary atoms located near the surface in the atomic region are often controlled as a boundary condition using the linear elastic solution. This study also adopts such a boundary condition. However, our previous study showed that very high strain occurs near the crack tip, and the initial mechanical properties may be changed under such a condition. Thus, the assumption of the linear elastic condition, that is, small-scale yielding condition, may not apply at a high loading level. In other words, the stress intensity factor $K$ that is given as the boundary condition based on the linear elastic solution can no longer correctly express the phenomenon of the mechanical field near the crack tip.

As already mentioned, many parameters describing the mechanical state near the crack tip have been proposed. The $J$ integral is one of the most representative of these parameters for conditions of large-scale yielding.

### 2. *Definition of* J*

The $J$ integral[7] is a representative parameter of the mechanical field near the crack tip, and it is defined in a continuum as a line integral along a path surrounding the crack tip as follows:

$$J = \int_{\Gamma}\left(W\delta_{1j} - \sigma_{ij}\frac{\partial u_i}{\partial x_1}\right)n_j \,\mathrm{d}\Gamma \tag{5}$$

where $W$, $\sigma_{ij}$, and $u_i$ are strain energy density, stress, and displacement, respectively. It is, however, difficult to estimate the line integral directly by using MD simulations of atomic models. By the introduction of a function $Q$, whose values are 0 and 1 on $\Gamma_1$ and $\Gamma_2$, respectively, in region $S^*$ that is surrounded by closed path $\Gamma^*$ as shown in Fig. 4, another form of integral $J^*$ is considered as follows:

$$\begin{aligned} J^* &= \int_{\Gamma^*}\left(W\delta_{1j} - \sigma_{ij}\frac{\partial u_i}{\partial x_1}\right)Q n_j \,\mathrm{d}\Gamma \\ &= \iint_{S^*}\left(\left(W\delta_{1j} - \sigma_{ij}\frac{\partial u_i}{\partial x_1}\right)Q\right)_{,j}\mathrm{d}S \end{aligned} \tag{6}$$

Equation (6) can be established for an arbitrary form of function $Q$ along $\Gamma_3$ and $\Gamma_4$ because the stress vector $\boldsymbol{t}_i = \sigma_{ij}n_j$ is vanished on crack surfaces $\Gamma_3$ and $\Gamma_4$.

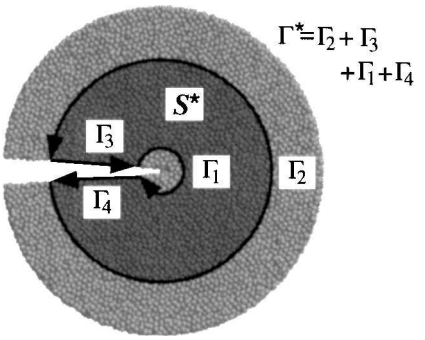


**Fig. 4 Integral path for $J^*$ integral of atomic model of amorphous metal.**

It is proved that $J^*$ is equal to $J$ by using the definition of $W$, the relationship of strain vs displacement, the symmetry of stress, and balance equations.[8] The mechanical state in the vicinity of the crack tip is studied here by direct calculation of

$$J^* = \iint_{S^*}\left(\left(W\delta_{1j} - \sigma_{ij}\frac{\partial u_i}{\partial x_1}\right)\right)\frac{\partial Q}{\partial x_j}\,\mathrm{d}S \tag{7}$$

### 3. *Estimation of* J *in the Atomic Model*

It is necessary to evaluate displacement, strain, and stress to estimate $J$ of amorphous metal. However, this is difficult because they are highly oscillating due to the random structure of their atomic levels. To avoid this difficulty, we propose that the object values at point P are obtained by taking the average over atoms that exist in the region far from a constant distance. The average is not taken by simple summation but is taken by weighted summation where a weighted function is used. Because the function must decrease with increasing distance from point P, we choose a normal distribution function that has appropriate variance.

By assuming that $W$ is calculated by the change of potential energy density $W^{(\alpha)}$, $J^*$ is calculated by

$$J^* = \sum_{\alpha \text{in} S^*}\left(\left(W^{C(\alpha)} - W^{O(\alpha)}\right)\delta_{1j} - \left(\sigma_{ij}^{C(\alpha)} - \sigma_{ij}^{O(\alpha)}\right)\frac{\partial u_i}{\partial x_1}\right)\frac{\partial Q}{\partial x_j}V^{(\alpha)}\frac{1}{l_z} \tag{8}$$

where $V^{(\alpha)}$ is the volume occupied by $\alpha$th atom and the values with superscripts $B$, $C$, and $S$ indicate the results of models B, C, and S, respectively. The values with superscript $O$ are the reference states, which are introduced to remove the influence of the initial stress and the increasing free surface energy by the introduction of the crack and to evaluate the increase of pure stress and pure strain energy as follows:

$$\sigma_{ij}^{O(\alpha)} = \sigma_{ij}^{B(\alpha)} \tag{9}$$

$$W^{O(\alpha)} = \begin{cases} W^{S(\alpha)} & (x < 0) \\ W^{B(\alpha)} & (x \geqq 0) \end{cases} \tag{10}$$

The unloaded cracked configuration cannot be used as the reference state because it becomes almost the same as model B. Although this idea is not necessarily precise near the $y$ axis, the surface effect can be removed.

The form of the weighted function $w$ may be choosen arbitrarily, and we adopt $w$ as the three-dimensional normal distribution whose origin is set at the evaluation point, and the standard deviation is determined as the length of cutoff distance of the interatomic potential function ($r_c = 3.57$ Å). Displacement gradients are calculated by the concept of distribution as follows:

$$\frac{\partial u_i}{\partial x_1}(w) = -\int_{-\infty}^{\infty}\int_{-\infty}^{\infty}\int_{-\infty}^{\infty} u_i\frac{\partial w}{\partial x}\,\mathrm{d}x\,\mathrm{d}y\,\mathrm{d}z \tag{11}$$

The following equation is actually used instead of Eq. (11):

$$\frac{\partial u_i}{\partial x_1} = -\sum_{\alpha=1}^{N} u_i^{(\alpha)}\frac{\partial w}{\partial x}V^{(\alpha)} \tag{12}$$

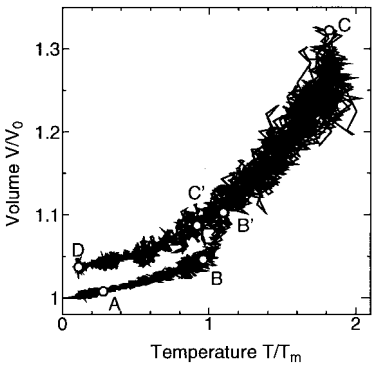


**Fig. 5 Relation of temperature and volume.**

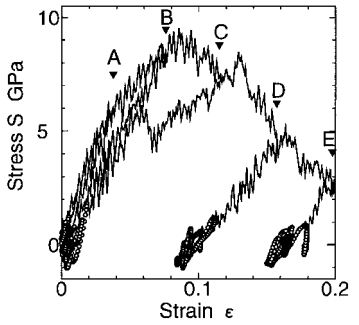


**Fig. 6 Stress–strain diagram (loading and unloading).**

## III. Analytical Result and Discussion

### A. Generation of Amorphous Structure

Figure 5 shows the relationship between volume and temperature during the melting–freezing process in case 1. In the region of low temperatures (A–B in Fig. 5), as the temperature rises, the volume gradually increases. However, the change of volume shows a discontinuous jump (point B). The temperature at this point is defined as the melting point $T_m$. In our adopted model, $T_m \simeq 2800$ K. After melting (B′–C), expansion continues at a rate of volume increase different from its solid state (A–B). In the quenching, the volume does not show discontinuous change even below the melting point (point C′) but condenses as a metastable supercooled liquid, and the rate of volume vs temperature changes in the vicinity of $T_g = 0.89T_m$ (glass transition temperature) (C′–D). A phase transition has taken place from liquid to solid at this point.

### B. Material Properties of Loading

*1. Material Properties of Preloading and Unloading*

Figure 6 shows the plotting of relations between Green–Lagrange strain and the second Piola–Kirchhoff stress in the first (pre)loading. It is certified by loading along other directions that the elastic property is almost isotropic.

In Fig. 6, the solid line indicates the route of load–unloading, and the open circles indicate the relaxation process. In the cases of unloading at points A, B, and C, the residual strains almost vanish, but at points D and E, large residual strains remain. This demonstrates that the large preloading has created obvious structural change.

For unloading points A, B, C, D, and E, the models generated by such calculations are named M1, M2, M3, M4, and M5, respectively. The material model initially obtained is referred to as M0. Figure 7 shows the change of the potential energy. The values of potential energy of models M4 and M5 are larger than that of the initial structure M0. This indicates that those structures have quasi-stable status. On the other hand, the volumes of all models are close to that of the initial structure. This means that these quasi-stable structures do not include the void that is one of the defects that increases the potential energy of surface energy.

*2. Behaviors in Reloading*

Next, uniaxial tensile deformation is again applied to the material models from M1 to M5. As earlier, the stress–strain curves, which are drawn as oscillated curves in Fig. 8, are given by the MD simulations of the uniaxial tensile deformation in models M1 and M5. The result obtained is that if the preloading is larger, Young's modulus becomes smaller. To consider the dependence of mechanical properties on the level of preloading, the stress–strain relationships given by the following models are used.

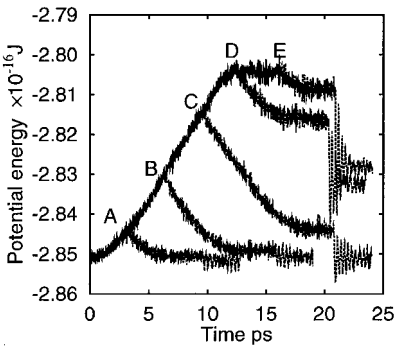


**Fig. 7 Change of potential energy for each model during processes of loading and unloading.**

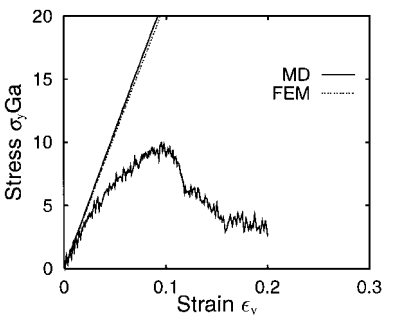


**M1**

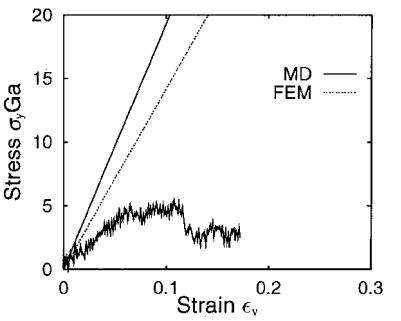


**M5**

**Fig. 8 Stress–strain relation (reloading).**

1) In this model, Young's modulus that is calculated by the microscopic elastic constant for the whole cell is obtained by MD for relaxation in each model; that is, it is an example of the law of mixture that is evaluated under the assumption that the local strain is equal to the strain of the whole cell. The stress–strain relationship with a gradient equal to this Young's modulus is shown as a straight line in Fig. 8.

2) By dividing the sides of the unit cell into eight equal parts, the unit cell consists of 512 eight-node solid elements. The elastic property of each element is given by the atomic elastic constant of the atom whose center of gravity is nearest to the center of the element. By the using of this model, tensile deformation analysis for the heterogeneous elastic body is carried out using the finite element method (FEM). By the relationship of load-displacement calculated by this analysis, the macroscopic Young's modulus and the external stress–strain relationships are obtained. This relationship of stress–strain is shown as a broken line in Fig. 8.

By comparing models 1 and 2, we see that whereas both stress–strain curves almost coincide in the model M1, the difference in model M5 is remarkable. This means that the elastic property is evaluated by the law of mixture in the material model M1, but this is no longer the case in material models such as M5 in which structures are changed by large preloading.

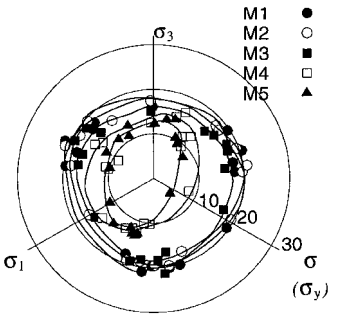


**Tensile reloading**

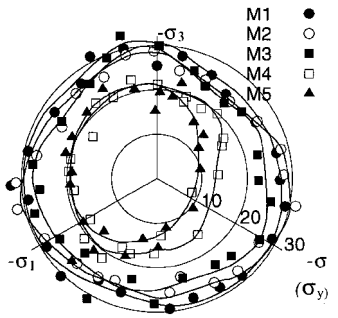


**Compressive reloading**

**Fig. 9 Yield points on Π plane.**

*3. Yielding Criterion*

Because amorphous metal exhibits no remarkable work hardening, the maximum load point can be regarded as the point where inelastic deformation begins. This is called the yielding point. In a case of multiaxial loading, the stress state that gives the maximum von Mises equivalent stress is regarded as the yielding point. The normal stress components $\sigma_x$, $\sigma_y$, and $\sigma_z$ can actually be regarded as the principal values, which are designated $\sigma_1$, $\sigma_2$, and $\sigma_3$, respectively. Thus, the yielding points estimated by the preceding methods are put on a plane, which is shown in Fig. 9. In the Π-plane, the radius from the origin stands for equivalent stress $\sigma_{eq} = \sqrt{3J_2}$ (where $J_2$ is the second invariant of the deviatoric stress). Whereas the yield loci on the Π-plane are nearly circular for M1, M2, and M3, remarkable decreases are recognized for M4 and M5 in the $y$ direction, which is the direction of the initial tensile loading. This indicates that M4 and M5 have received a certain amount of anisotropic damage.

*4. Elastic Constant Matrix and Its Determinant for Mode I Cracks*

The tensile direction component of each atomic elastic constant matrix and the determinant of the matrix are evaluated for each material model to examine the change of structure caused by preloading.

Figure 10 shows the distribution of a value of the diagonal component $C^{(i)}_{2222}$ of the atomic elastic constant matrix most closely related to the property of tensile direction for M0 and M5. Figure 11 shows the distribution of the value of the determinant of the atomic elastic constant matrix.

In Figs. 10 and 11, the white bars indicate the overall distribution of atoms in the system, and the shaded bars indicate the distribution of the atoms located centrally in (0,0,12,0)-type Voronoi's polyhedra. These exist as typical structures that are locally stable in amorphous metal. According to Fig. 10, in the case of the model subjected to preloading, the shape of distribution of all atoms and their average value (that is, the macroscopic elastic constant of the whole cell evaluated by the law of mixture) is hardly different from the initial model. Nevertheless, according to Fig. 11, it is shown that as the intensity of preloading increases, the number of atoms at which the values of the determinant are small increases.

Therefore, the reason that the stress–strain relationship for M5 obtained by FEM and MD analyses is largely different from those obtained by the law of mixture (see Fig. 8) is related to the number of unstable atoms with weak stiffness increasing.

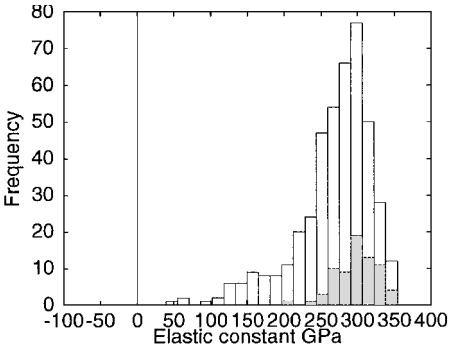


**M0**

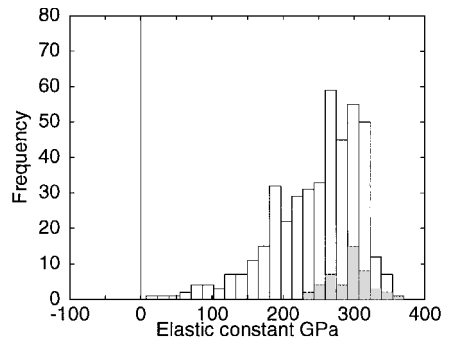


**M5**

**Fig. 10 Component $C^{\alpha}_{2222}$ of atomic elastic constant.**

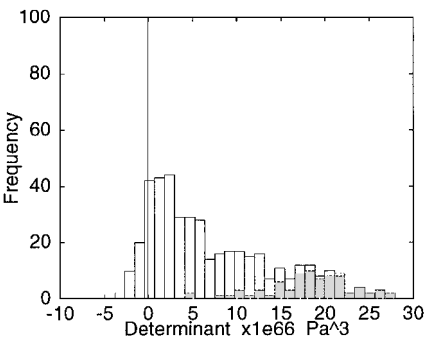


**M0**

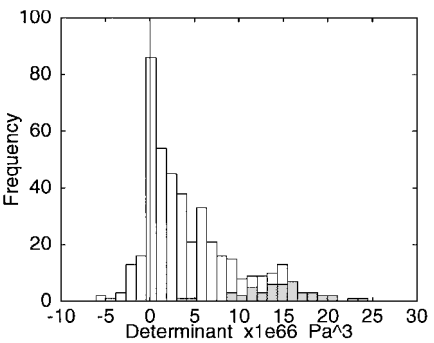


**M5**

**Fig. 11 Determinant of the atomic elastic constants matrix $|C|$.**

### C. Evaluation of *J* integral

*1. Strain Energy Density, Stress, and Displacement*

The strain energy density $W^{C(\alpha)} - W^{O(\alpha)}$, the stress $\sigma_y^{C(\alpha)} - \sigma_y^{O(\alpha)}$, the displacement $u_x^{(\alpha)}$, and the displacement gradient $du_x^{(\alpha)}/dx$ that are evaluated by MD simulation of atoms existing near the $x$ axis ($-3 < y < 3$ Å) and the linear elastic solutions for the position of the same atoms are shown in Fig. 12. The theoretical solution is evaluated at each atomic site, whose $y$ coordinate is not strictly zero, and so theoretical plots are scattered. The tendencies of the distributions

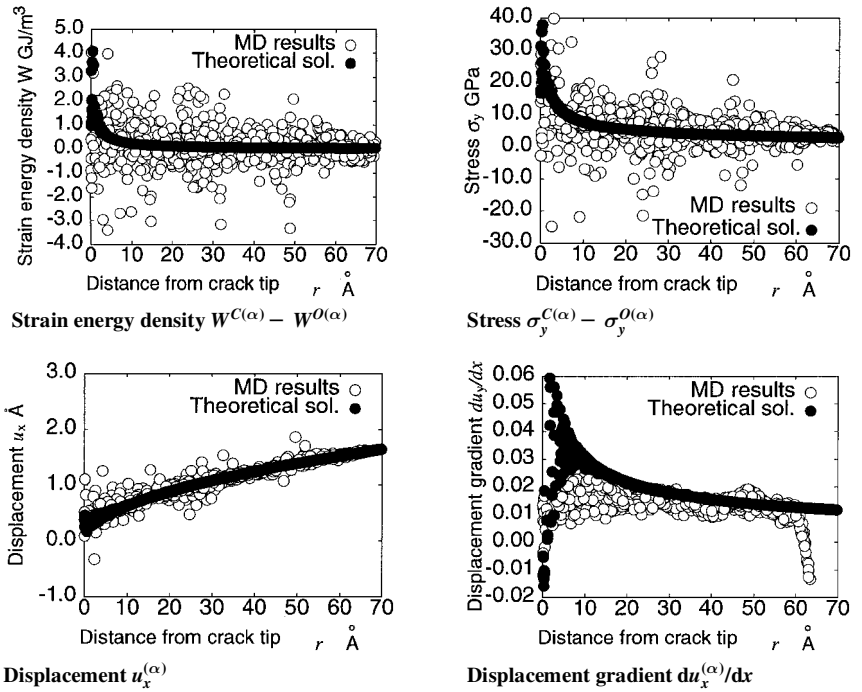


**Fig. 12 Mechanical values obtained using results of MD analysis (model C).**

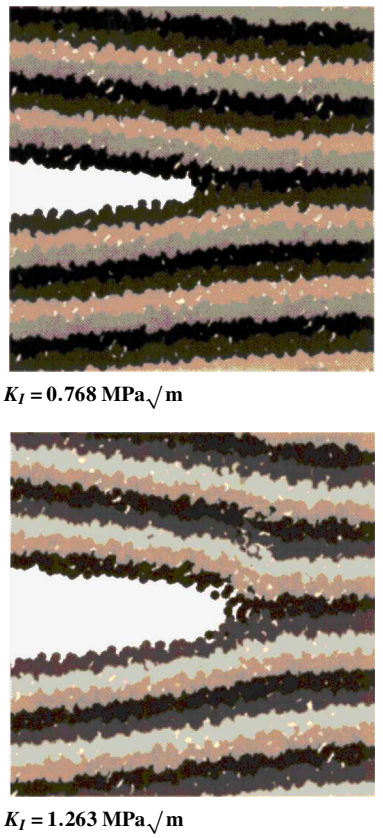


**Fig. 13 Rearrangement of atoms near crack tip.**

obtained by these MD simulations show strong agreement with the linear elastic solution, except in the vicinity of the crack tip.

*2. Rearrangement of Atomic Structures near the Crack*

Figure 13 shows the rearrangement of atomic structure near the crack tip during deformation. For easy understanding of the deformation, atoms are shaded corresponding to the $y$ coodinates initial position. As the deformation becomes larger, the crack extends and becomes blunted, and localized shear deformations are observed.

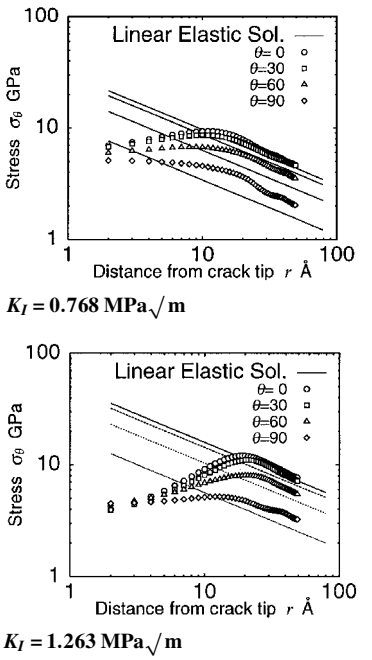


**Fig. 14 Distribution of radial stress near crack tip (logarithm plot).**

*3. Change of Stress Distribution by Loading*

Figure 14 shows the logarithm relationships between the stress $\theta$ and distance $r$ from the crack tip along radial directions that are measured at 0, 30, 60, and 90 deg counterclockwise from the crack progress direction. When the load is small, the relationships agree with the linear elastic solution except for the very narrow region near the crack tip in which the material has become inelastically damaged. The approximation to an elastic body is available at a few angstroms from the crack tip, even in the case of $K_I = 1.263$ MPa $\cdot$m.

*4. $J^*$ Integral Under Large Mode I Deformation*

The dependencieson $J^*$ integralpath for four models (from C to I) that are subjected to the different levels under mode I deformation are shown in Fig. 15. The nominal $J^*$ values based on the linear elastic solution evaluated by Eq. (3) are shown as solid lines in

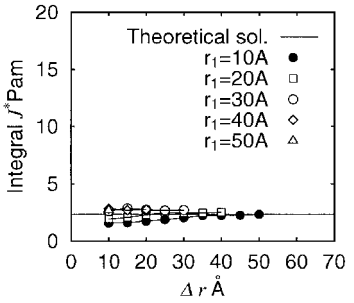


**a) Model C ($K_I = 0.606$ MPa$\sqrt{m}$)**

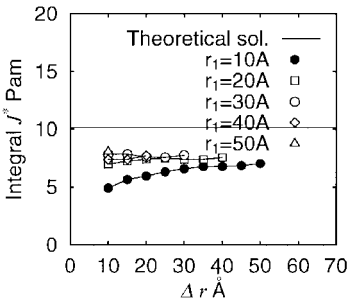


**b) Model H ($K_I = 1.263$ MPa$\sqrt{m}$)**

**Fig. 15 Dependence of integral path for $J^*$.**

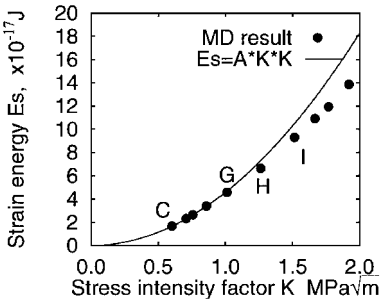


**Fig. 16 Loading level dependence of strain energy.**

Fig. 15. In the cases where $K_I$ values are small (Fig. 15a), the dependencies on the $J^*$ integral path almost vanish. However, the $J^*$ value decreases remarkably when $K_I$ becomes large (Fig. 15b) and $r_1$ becomes small.

By comparing these results and Fig. 14, a remarkable decrease of the $J^*$ integral value occurs in the case of the $J^*$ integral path going through the nonlinear region where $r_1$ is small. However, even in the case where the region near the crack tip is nonlinear, if the $J^*$ integral path is taken some distance from the crack tip (within the elastic region), it has little dependency on the $J^*$ integral path. The $J^*$ integral value converges more, due to the larger width of the integral path, which is smaller than the nominal value predicted by Eq. (3) under large deformation. This means that the nominal value is no longer as large as the true value because of the nonlinearity caused by deformation and damage near the crack tip.

*5. Load Level Dependency of Strain Energy*

Figure 16 shows the relations of stress intensity factor $K_I$ and strain energy, for all 10 analyzed crack models that are subjected to different loads. The solid curve drawn in Fig. 16 is the curve fitting $E_s = A \cdot K_I^2$, and it indicates the values predicted from the linear elastic solution, where constant $A$ is selected as the solid curve that goes through the origin and the point for model C. Here, the point for model C is assumed as the mechanical value near the crack tip based on the linear elastic solution.

According to Fig. 16, when $K_I$ is small, the strain energies obtained by the MD simulation agree with the value predicted by the linear elastic solution. However, when $K_I$ is larger than the value of model G, the strain energies are smaller than the value predicted by the linear elastic solution. In the case of model H, the $J^*$ integral calculated by taking $r_1 = 10$ Å (i.e., taking the integral path as near the crack tip) begins to deviate from the results of other paths, as shown in Fig. 15b. Though mechanical properties are changed in the region near the crack tip where material is damaged by high stress, we can predict the mechanical state surrounding the crack tip by using the $J^*$ integral calculated by choosing the appropriate integral path that avoids the damage zone.

## IV. Conclusion

An atomic arrangement of amorphous iron was created by MD, and simulations were carried out for material testing. The $J$ integral values under mode I loading were analyzed to evaluate the true mechanical fields near the crack tip.

1) The amorphous structure was generated by the simulation of a rapid-quenching process.

2) Amorphous iron recovers the initial properties even if it is subjected to strain approaching the maximum stress, but an excess loading induces a definite atomic rearrangement (damage) that causes a remarkable decrease of the elastic modulus and strength (yielding stress).

3) The yielding point in multiaxial stress is described by $J_2$ when the damage in the preloading is light and the tensile hydrostatic component of stress decreases the yield stress.

4) Near the crack tip field, the mechanical properties were changed by the nonlinearity properties of the material and atomic rearrangement of cleavage and blunting.

5) $J$ integrals were evaluated as $J^*$, and the mechanical damage caused by the change of internal mechanical properties was evaluated in detail by $J^*$ calculated on an appropriate integral region avoiding the process zone.

## Acknowledgment

Keiko Nakatani and Hiroshi Kitagawa would like to acknowledge support by the Grant-in-Aid for Scientific Research through the Ministry of Education, Science, and Culture, Japan.

## References

[1]Masumoto, T., and Maddin, R., "Structural Stability and Mechanical Properties of Amorphous Metals," *Materials Science and Engineering*, Vol. 19, No. 1, 1975, pp. 1–24.

[2]Maddin, R., and Masumoto, T., "The Deformation of Amorphous Palladium-20 at.% Silicon," *Materials Science and Engineering*, Vol. 9, 1972, pp. 153–162.

[3]Allen, M. P., and Tildesley, D. J., *Computer Simulation of Liquids*, Clarendon, Oxford, 1987, pp. 71–109.

[4]Finnis, M. W., and Sinclair, J. E., "A Simple Emprical *N*-Body Potential for Transition Metals," *Philosophical Magazine, A*, Vol. 50, No. 1, 1984, pp. 45–55.

[5]Finnis, M. W., and Sinclair, J. E., Erratum, *Philosophical Magazine, A*, Vol. 53, No. 1, 1986, p. 161.

[6]Parrinello, M., and Rahman, A., "Polymorphic Transitions in Single Crystals: A New Molecular Dynamics Method," *Journal of Applied Physics*, Vol. 52, No. 12, 1981, pp. 7182–7190.

[7]Rice, J. R., "A Path Independent Integral and the Approximate Analysis of Strain Concentration by Notches and Cracks," *Journal of Applied Mechanics*, Vol. 35, 1968, pp. 379–386.

[8]Li, F. A., Shih, C. F., and Needleman, A., "A Comparison of Methods for Calculating Energy Release Rates," *Engineering Fracture Mechanics*, Vol. 21, 1985, pp. 405–421.

G. A. Kardomateas
*Associate Editor*